Structural and chemical characterization of SnO_2-based nanoparticles as electrode material in Li-ion batteries

Dorothée Vinga Szabó · Goran Kilibarda · Sabine Schlabach · Vanessa Trouillet · Michael Bruns

Abstract Improvement of long-term stability of electrode materials in Li-ion batteries requires a detailed understanding of influence of synthesis parameters on surface chemistry and on properties. Therefore, bare SnO_2 and core/shell nanoparticles with SnO_2 core and a hydrocarbon shell are synthesized in an Ar/20% O_2 microwave plasma, deposited as porous nanoparticle films in situ on heated Ni-substrates, and finally assembled as anodes in Swagelok cells. In a comprehensive study, we investigate structure, particle size, chemistry, morphology, and water content of the nanoparticles using X-ray diffraction, transmission electron microscopy, specific surface area analysis, and coulometric water titration. The thicknesses of the nanoparticle films and their surface chemistry are investigated by scanning electron microscopy and X-ray photoelectron spectroscopy. SnO_2 nanoparticles are crystalline, with a tetragonal cassiterite structure. Primary particle sizes around 3 nm are reached for the bare SnO_2 particles, 5 8 nm for the cores of the core/shell nanoparticles. A minimum microwave power of 900 W is necessary to synthesize SnO_2 nanoparticles without precursor residuals as pristine SnO_2 particles for the subsequent coating step. In the coating step increasing hydrocarbon content can be correlated with increasing carbon-precursor feeding rate. Water uptake, stemming either from the process, or due to atmospheric contamination, can successfully be reduced by a thermal treatment. The still remaining water is a function of specific surface area. Finally, bare SnO_2 versus core/shell nanoparticles are compared regarding the influence of the shell on the electrochemical properties. The principal improved functionality of the developed anodes in Swagelok cells is demonstrated.

D. V. Szabó (✉) · G. Kilibarda · S. Schlabach · V. Trouillet · M. Bruns
Institute of Applied Materials Materials Process Technology, Karlsruhe Institute of Technology, Hermann von Helmholtz Platz 1, 76344 Eggenstein Leopoldshafen, Germany
e mail: dorothee.szabo@kit.edu

G. Kilibarda
Department of Microsystems Engineering, Albert Ludwigs University of Freiburg, Georges Koehler Allee 102, 79110 Freiburg, Germany

Introduction

Tin dioxide (SnO_2)-based materials are widely discussed as interesting anode material for Li-ion batteries [1 8]. The maximum theoretical reversible specific capacity of SnO_2 with ca. 780 mAh/g is more than twice as high as the capacity of nowadays used graphite anodes, featuring a specific reversible capacity of 372 mAh/g [6, 7, 9]. SnO_2 is a conversion material, forming metallic Sn in a first, irreversible step, followed by a reversible alloying and de-alloying process of Li^+ with metallic Sn. However, the conversion is accompanied by the side effect of volume expansion larger than 200%, leading to strong capacity fading due to crack formation and loss of electrical contact between particles during charging/discharging. Using nanomaterials exhibit the advantage of enhanced Li-insertion/removal, due to the short distances in small particles. Furthermore, nanomaterials are expected to overcome the problem of electrode deterioration [10, 11]. Improved capacity of nanosized SnO_2 compared to micron-sized SnO_2 has been demonstrated e.g., by Chen et al. [12]. Also encapsulation of SnO_2-nanoparticles with a carbon containing scaffold [8], or application of either SnO_2-graphene nanocomposites [13, 14] or SnO_2/C

core/shell nanoparticles [15] seem a promising way for improved capacity.

Improving capacity of electrode materials by reducing dimensions of the materials in use is one aspect of the optimization process. However, one problem occurring while applying nanomaterials is the large specific surface area: this surface is susceptible to surface contamination and water adsorption during the materials synthesis process, and transfer processes from synthesis equipment to glove box for cell assembly. This topic is barely discussed in literature, although several research groups use wet-chemical methods combined with chloride precursors for materials synthesis [2, 3, 5, 7, 12, 14]. Gas phase synthesis methods as the one developed in our research group seem more promising for the synthesis of nanostructured anode materials [8, 16, 17], because they do not use additional water or solvents.

Our approach is to use nanocomposites made of core/shell nanoparticles with an active core of SnO_2 and a stabilizing and conducting shell, e.g., carbon, acting also as a scaffold between the core particles. We expect such materials to benefit from their nanoporous morphology featuring locally free space to compensate volume changes during the charging/discharging process. Due to the double bonds, dicyclopentadiene, $C_{10}H_{12}$, is expected to be a favorable precursor for the formation of elemental carbon or even graphite in the plasma. Several articles report that graphite formation is possible in inert-gas plasmas and microwave plasmas [18 20]. The synthesis of amorphous C:H films by plasma-enhanced CVD was also reported [21], as well as the formation of carbon spheres by low temperature pyrolysis of cyclic hydrocarbons [22].

In this study, we report our investigation on porous SnO_2-based nanoparticle films without carbon black or any additional binder and slurry. The proof of concept for this type of materials has already been done [8], with results comparable to literatures [3, 5, 14, 23]. For the synthesis of SnO_2-based nanoparticles a microwave plasma process is applied [16] combined with in situ deposition on preheated substrates [8, 17]. We study the influence of different synthesis parameters on particle size, structure, and morphology, as well as on composition. In addition, bare SnO_2 versus core/shell nanoparticles are compared regarding the influence of a carbon containing coating on the electrochemical properties. The particle and film characterization is done using complementary analytical methods to understand the processes occurring during materials synthesis in an Ar/20% O_2 plasma and problems during cell assembling. With this understanding, optimization of nanomaterials synthesis coupled with improved cell assembly should be feasible. The final aim is to develop SnO_2-based nanomaterials with significantly improved long-term cycling stability.

Experimental

Material synthesis and film deposition

The Karlsruhe microwave plasma process (KMPP) was used for the synthesis of bare SnO_2 and core/shell nanoparticles with SnO_2 core and hydrocarbon shell. Water-free tetra-*n*-butyltin, $Sn(C_4H_9)_4$ (ABCR, Karlsruhe, Germany), is used as precursor for the synthesis of SnO_2 nanoparticles, and dicyclopentadiene, $C_{10}H_{12}$ (Fluka, Buchs, Switzerland), is used as the precursor for the shell. All precursors are liquid, and therefore can be fed with a syringe pump. Core/shell nanoparticles have been synthesized using two consecutive plasma zones. System pressure was set to 10 mbar, reaction gas was a mixture of 80 vol% Ar/20 vol% O_2 with a gas flow rate of 5 l/min, carrier gas for precursor transport was Ar with a flow rate of 0.5 l/min in all cases, respectively. Feeding rates of the precursors, and microwave power were varied (core particle: 2.0 5.0 ml/h, 600 900 W, shell: 0.5 12 ml/h, 340 W).

For the utilization as negative electrode material in Li-ion batteries the nanoparticles have been deposited in situ as a porous nanoparticle film on 200 °C preheated Ni-substrates according to the method described in previous study [17]. Furthermore, powder for additional analysis was collected by thermophoresis. In the case of subsequent drying of the films and powders this was done at 140 °C for 2 h. The in situ deposited nanoparticle films were directly assembled in Swagelok half-cells, without any additional carbon black or binder, in an Ar-filled (0.5 ppm O_2, 0.5 ppm H_2O) Unilab glove box (MBraun, Garching, Germany) using a Li metal counter electrode, a porous separator, a standard electrolyte of 1 M $LiPF_6$ solution in a 1:1 mixture of ethylene carbonate (EC) and dimethyl carbonate (DMC) (Merck, Darmstadt, Germany), and the same compacting pressure.

Characterization of nanopowders and nanoparticle films

The nanoparticles were examined by analytical transmission electron microscopy (TEM) including selected area electron diffraction (SAED), and electron energy loss spectroscopy (EELS) regarding structure, chemical composition, particle morphology, and size. A Tecnai F20ST (FEI, Eindhoven, The Netherlands), equipped with a GATAN Multiscan CCD with GIF (Gatan, Pleasanton, CA, USA) was used, operating at 200 kV. Sample preparation was done by dipping Cu grids with lacey carbon films into the powders. EELS was performed in the image mode using a magnification of 17 k. The full width half maximum (FWHM) of the zero loss peak was 1.2 1.5 eV. The spectrometer dispersion was set to 0.3 eV/channel. The relative sample thicknesses were determined by log-ratio method to be $t/\lambda < 1$ in all cases. Special care was taken for the acquisition of EEL spectra, to

analyze sample areas in the film holes, avoiding influence of surrounding carbon. In addition, particle characterization was done by X-ray diffraction (XRD) using a Philips X'Pert (PANalytical, Almelo, The Netherlands). Water content of the powders was investigated by coulometric water titration, using a 731 Karl-Fischer Coulometer with 860 KF Thermoprep (Metrohm, Filderstadt, Germany). The specific surface area was determined by Brunauer Emmet Teller method (BET) using a Flow Sorb II 2300 from Micromeritics Instruments Corporation (Norcross, GA, USA) in 70% He/30% N_2 as carrier gas.

The nanoparticle films were investigated by scanning electron microscopy (SEM) using a ZEISS Supra-55 (Zeiss, Oberkochen, Germany) regarding their film morphology and thickness. X-ray photoelectron spectroscopy (XPS) measurements were performed using a K-Alpha XPS spectrometer (ThermoFisher Scientific, East Grinstead, UK). Data acquisition and processing using the Thermo Avantage software is described elsewhere [24]. All samples were analyzed using a microfocused, monochromated Al Kα X-ray source (30 400 μm spot size). The K-Alpha charge compensation system was employed during analysis, using electrons of 8 eV energy and low-energy argon ions to prevent any localized charge build-up. The spectra were fitted with one or more Voigt profiles (binding energy uncertainty: $\pm$0.2 eV). The analyzer transmission function, Scofield sensitivity factors [25], and effective attenuation lengths (EALs) for photoelectrons were applied for quantification. EALs were calculated using the standard TPP-2M formalism [26]. All spectra were referenced to the C 1s peak of hydrocarbon at 285.0 eV binding energy controlled by means of the well-known photoelectron peaks of metallic Cu, Ag, and Au.

Cyclic voltammetry, using a Zahner Zennium electrochemical workstation with XPOT (Zahner Messsysteme, Kronach, Germany), is applied for first electrochemical tests in the scan range from 0.0 to 3.0 V and a scan rate of 0.05 mV/s. Specific charge and discharge capacity was acquired with a Lithium cell cycler (LICCY, developed at Karlsruhe Institute of Technology, Institute for Data Processing and Electronics) in the voltage range from 0.1 to 2.8 V and a constant current of 39.1 mA/g, corresponding to a charge/discharge rate of C/20. The active mass was determined by weighting the amount of material deposited on the substrate combined with gravimetric analysis of the corresponding powder.

Results and discussion

Microscopic and structural characterization

One of the main advantages of the microwave plasma process is that the low intrinsic reaction temperatures and the short residence times in the plasma zone lead to particle sizes below 10 nm with coeval narrow particle size distribution. This was shown for several oxide nanoparticles in the past [16, 27 30], and also for SnO_2 nanoparticles for gas sensing applications [17, 31]. Moreover, we have already proven that KMPP is appropriate to synthesize SnO_2/SiO_2 core/shell nanoparticles [32] and oxide/polymer core/shell nanoparticles [33 35]. The cores from the first synthesis step act as nuclei for the condensation of the second phase. From our earlier XPS experiments it is known that SnO_2 nanoparticles made from $SnCl_4$ exhibit residual Cl, obviously stemming from the precursor. A heat treatment at 300 °C for 3 days is necessary to reduce residual Cl below XPS detection limit [17]. However, Cl is not favorable in the Li-ion battery, as it is damaging the Swagelok cell, respectively, battery, due to the formation of HCl. To get rid of these problems, we favor $Sn(C_4H_9)_4$ as a metal-organic precursor for the synthesis of SnO_2 nanoparticles. Particles produced in such manner can be directly and solvent-free deposited onto nickel substrates and form mechanical stable porous layers of columnar structure with thicknesses up to 8 μm, proven by SEM images in Fig. 1.

XRD and SAED clearly show tetragonal cassiterite structure of the nanoparticles. As expected, TEM investigations of the SnO_2 nanoparticles made from $Sn(C_4H_9)_4$ reveal also spherical and crystalline particles, with a slight

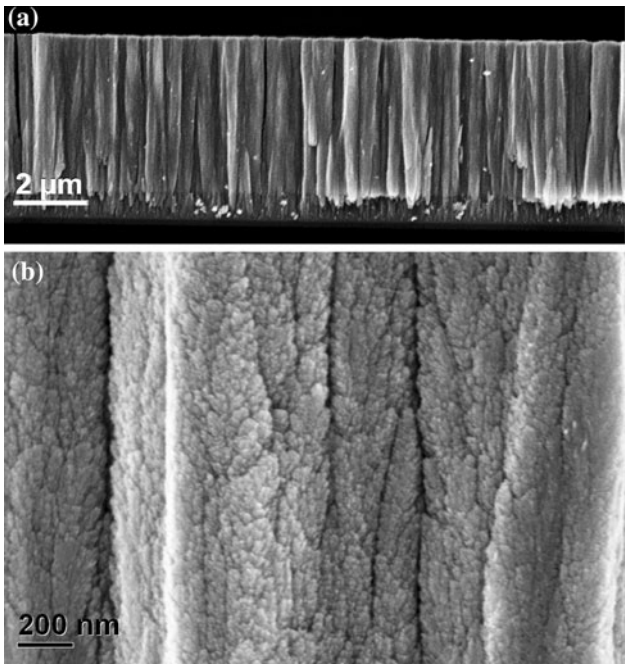

Fig. 1 SEM image (side view) of a SnO_2 nanoparticle film made from $Sn(C_4H_9)_4$ precursor with a feed rate of 2 ml/h at 900 W microwave power in lower magnification (**a**) and higher magnification (**b**). The thickness of the film is around 8 μm after a deposition time of 15 min. The columnar and porous structure can be seen

dependency of particle size from precursor feeding rate. This is in agreement with earlier results [17, 31] for SnO_2 made from $SnCl_4$. Figure 2 shows a representative XRD image (a), TEM image (b), low loss and background corrected core loss EEL spectra (c) of bare SnO_2 nanoparticles synthesized at 600 W microwave power from $Sn(C_4H_9)_4$. The general features of the low loss EEL spectra are in good agreement with SnO_2 low loss spectra recorded by Powell [36]. Interband transitions are observed around 12.5 eV, the main bulk plasmon peak appears around 19 eV, and the Sn-$N_{4,5}$ peak appears around 32 eV. A slight broadening of the spectra combined with a loss of features is observed with decreasing particle size. A well-defined peak at 27 eV, characteristic for SnO [37], does not appear clearly; however, a small shoulder can be observed in the case of 2 3 nm particles, potentially indicating some SnO at the particle surfaces.

SAED images show continuous ring pattern without discrete spots and quite broad ring width for all samples. Thus, XRD, SAED, and TEM images indicate consistently small crystallite sizes. From the TEM image (Fig. 2b), a particle size of approximately 3 nm can be estimated. Lattice fringes clearly show crystallinity of the particles. The inset shows a digitally filtered particle with [110] and [101] fringes with 0.33 and 0.26 nm. A widespread SAED analysis of several SnO_2 powders synthesized under different conditions shows a clear trend with respect to lattice parameters: nearly, all samples exhibit the lattice parameter of the *a*-axis slightly smaller, and the lattice parameter of the *c*-axis slightly larger than the corresponding values from JCPDS data [38]. In general this is interpreted as an indication for oxygen vacancies, vacancy clusters, and local lattice disorder leading to an increase in *c* and a decrease in *a* [39]. Similar tetragonal distortion effects have already been found for nanostructured SnO_2 synthesized with a hydrothermal method, and particle diameters in the same order of magnitude [39]. A distinct dependency of lattice parameters on precursor concentration cannot be deduced for the investigated samples.

TEM and XRD investigations of our core/shell nanoparticles show slightly larger core sizes compared to the bare SnO_2 particles. This is due to the fact that particles pass a second plasma stage, where, besides coating with a second phase, obviously particle growth of the cores occurs due to collisions between SnO_2 cores. Figure 3 shows a representative TEM image (Fig. 3a) and an XRD image (Fig. 3b) of core/shell nanoparticles. The difference to bare SnO_2 nanoparticles (see Fig. 2) is evident: the SnO_2 cores appear like "embedded in a matrix". In the diffraction image, the peaks are narrower and more pronounced,

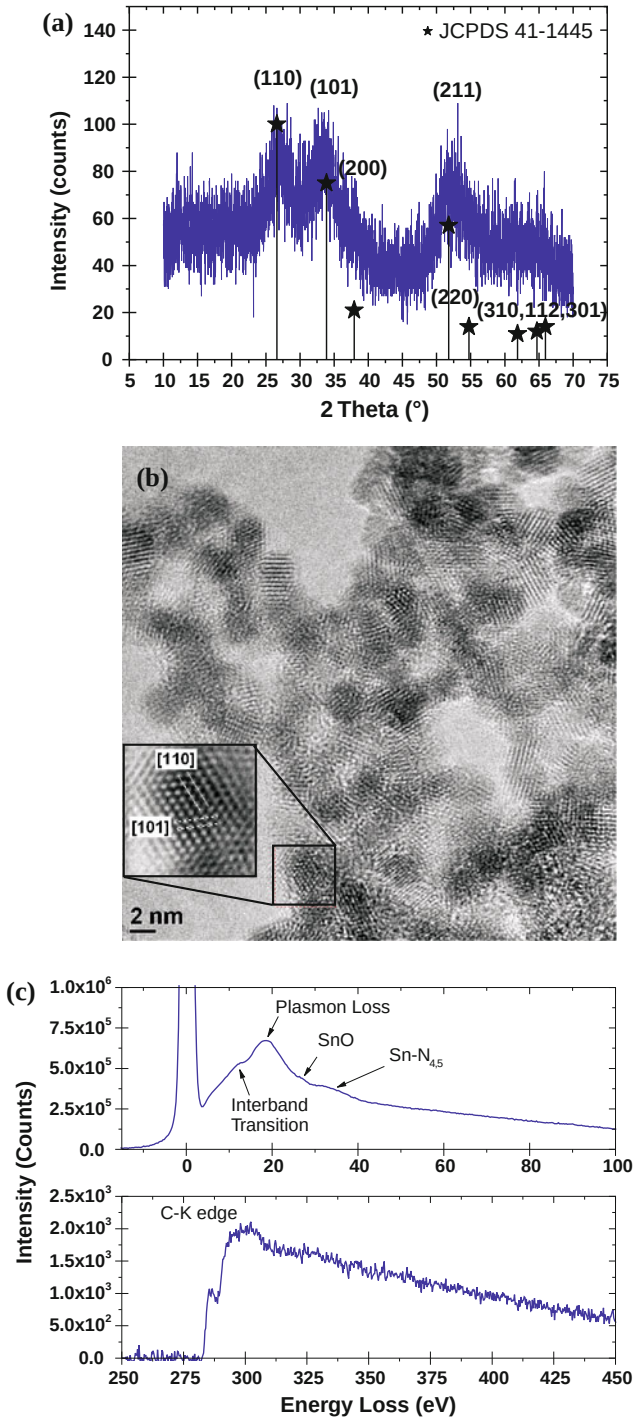

Fig. 2 **a** XRD image of SnO_2 nanoparticles made from $Sn(C_4H_9)_4$ precursor with a feed rate of 5 ml/h at 600 W microwave power. The *asterisks* reference diffraction data from JCPDS [36] of cassiterite. **b** TEM bright field image of SnO_2 nanoparticles. The filtered high resolution insert shows the [110] and [101] fringes with a spacing of 0.33 and 0.26 nm, respectively. **c** Low loss EEL spectrum and background subtracted C core loss EEL spectrum. The core loss EEL spectrum clearly shows the presence of carbon

indicating larger crystal size of the SnO_2 particles. The SnO_2 core size is around 5 8 nm, measured from TEM images. The shell, appearing as "matrix" seems to be amorphous, although double bonds of the precursor should boost graphite formation. The EELS low loss spectrum shows smeared characteristics, due to the overlapping of SnO_2 and C features: it cannot be distinguished between SnO_2 plasmon at ca. 19 eV, and C plasmon at 22 eV. In contrast, the C K edge at 283 eV is pronounced and a clear indication for the presence of C.

Characterization of nanoparticle surfaces

To prove a successful coating with an organic or a C shell a prerequisite is to produce carbon-free core particles. However, for SnO_2 particles prepared at 600 W microwave power XPS reveals aside the expected Sn and O a high amount of C. Analogous to the results from $SnCl_4$-based SnO_2 nanoparticles, we assume the C content to be a residual from the metal organic precursor. This is justified reliably by investigations of particles made from $Sn(C_4H_9)_4$ with different synthesis parameters (see Fig. 4). The detected components in the C 1s spectra are assigned to hydrocarbons (C 1s at 285.0 eV), to C O/C O C groups (C 1s at 286.4 eV), and to O C=O at 289.1 eV. They are in a good agreement with literature data [40 43]. In case of 900 W microwave power the C 1s components are significantly reduced. The oxidized carbon components obviously are due to uncompleted reaction of the organic precursor content with the reactive carrier gas.

However, as the particle size of about 3 nm is in the range of the XPS sampling depth, it is impossible to resolve whether the carbon content is spread across the complete core or already forms a shell. The increase of microwave power to 900 W, which in parallel means increasing the ionization degree in the plasma and the synthesis temperature, obviously is applicable to reduce the carbon components close to the detection limit of XPS, (see Fig. 4), even at higher feeding rates of the precursor. This weak residual carbon content might be also due to adventitious carbon contamination and therefore 900 W is obviously the minimum microwave power to synthesize precursor-free particles and assure a shell formation in the subsequent synthesis step. The O 1s component at 532.7 eV probably originates from water adsorption as the binding energy also can be attributed to, e.g., crystal water [44]. The binding energies measured for the tin oxide particle (Sn $3d_{5/2}$ at 487.4 eV, and O 1s at 531.3 eV) are in a good agreement with reference data and values reported in literature [32, 45].

In the XPS spectra of the core/shell particles similar C 1s components (C H, C OH, and O C=O) as in the case of bare SnO_2 are to be found. As the increase of the $C_{10}H_{12}$ precursor feeding rate directly results in an increase of mainly hydrocarbons, shown in Fig. 5, a successful coating

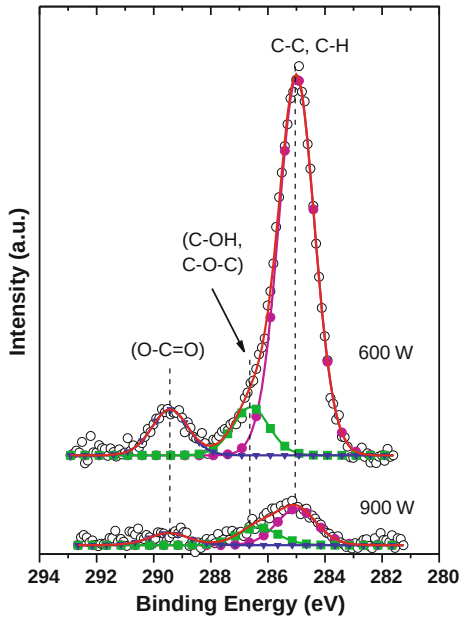

Fig. 4 XPS spectra: comparison of C 1s peaks from SnO_2 nanoparticle films, synthesized from $Sn(C_4H_9)_4$ with precursor feeding rate of 2.0 ml/h at 600 W and feeding rate of 5 ml/h at 900 W microwave power, respectively. For better visibility the spectra are stacked. *Black open circles* mark experimental data

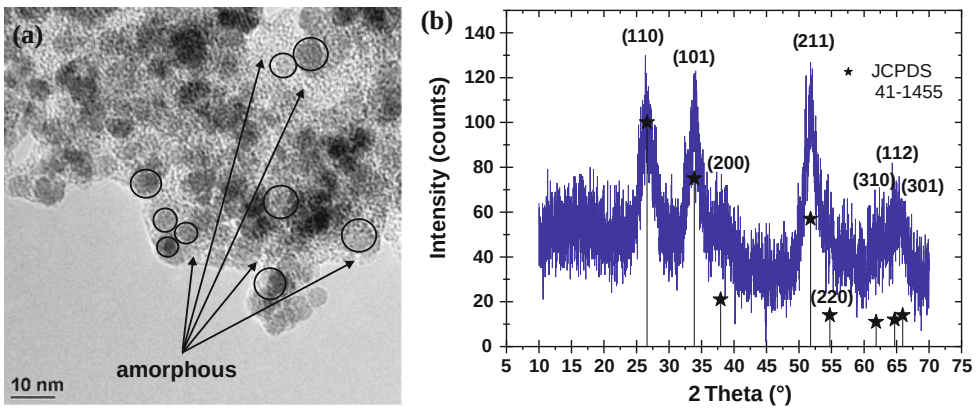

Fig. 3 **a** TEM bright field image and **b** XRD image of core/shell nanoparticles made from $Sn(C_4H_9)_4$ precursor (SnO_2 core) and $C_{10}H_{12}$ precursor (shell). *Arrow marks* amorphous appearing areas, *circles* single SnO_2 cores

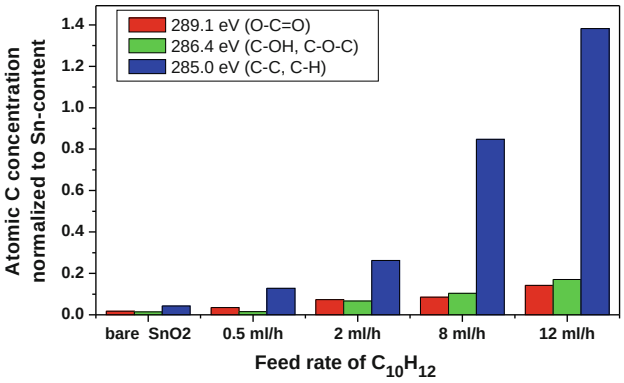

Fig. 5 Evaluated XPS C 1s data for different core/shell nanoparticle films made from $Sn(C_4H_9)_4$ precursor (SnO_2 core) and $C_{10}H_{12}$ precursor (shell). The feeding rate for the core precursor was kept constant with 5 ml/h, the feeding rate for the shell precursor was varied (0.5, 2, 8, and 12 ml/h, respectively). For comparison, data of the bare SnO_2 nanoparticles are also shown. The particles were synthesized using 900 W/340 W microwave power for core/shell, respectively. A successful coating with C_xH_y can be deduced

of the SnO_2 particle with an organic shell C_xH_y can be concluded. However, evidence of elemental carbon is not found. Whereas Qiao et al. [15] detect elemental carbon in SnO_2/C core/shell nanoparticles made by a one-pot solvothermal method.

Water determination

To address possible influence of water adsorption during our synthesis (due to H in the precursor, and possible oxidation of H in the Ar/20% O_2 plasma) and sample transport to cell assembling, as-produced powders, powders stored in ambient atmosphere and dried powders were compared. The water content of SnO_2/C_xH_y nanoparticles directly after the synthesis (collected by thermophoresis on a cooled surface and sealed under argon immediately after synthesis) is around 1.3 wt%. Additional drying reduces the water content below 0.5 wt%, meaning that water stemming from the process can be reduced by appropriate heating. As in contrast to the powder samples the nanoparticle films are deposited on 200 °C preheated substrates, adsorption of process water can be excluded at this point.

Water uptake in atmosphere is a severe problem when using nanoparticles for Li-ion battery. Although it is expected that nanosized electrode materials show better storage capacity due to the very short diffusion paths [10, 11], in parallel with decreasing particle size, the specific surface area increases, and consequently adsorption of atmospheric components and moisture increases [46]. In addition, it is well known that with decreasing particle size curvature radius increases, leading to a decreased vapor pressure. Water evaporation of strong bent surfaces is more difficult as water is strongly bonded to the small particles [47]. Nevertheless, water uptake of nanoscaled electrode materials is rarely a topic of scientific papers. The importance to account for water content can be deduced from Karl-Fischer titration of several as-produced powders after synthesis and storage under ambient conditions. In this case, distinct water contents between 5 and 10 wt% are detectable. In contrast, the initial water content of commercial SnO_2 powders stored in ambient air is significantly lower as these samples exhibit a considerable smaller specific surface area (particle sizes 50 100 nm). Heating the as-produced powders at 140 °C for 2 h reduces water content below 1 wt% in all cases. This is shown for several samples and types of materials in Fig. 6 as a function of experimentally determined specific surface area. The water content after drying can be correlated with the measured specific surface area. A notably particle growth is not expected under these conditions, as from earlier investigations it is known that bare SnO_2 nanoparticles exhibit only slight particle growth at 300 °C, and the particle growth of core/shell particles is even reduced at this temperature [17]. These results show the importance of careful drying the materials in use before assembling them to a battery cell. Furthermore, the results also demonstrate the occurring inherent problems using nanoparticles with particle sizes below 10 nm. As a low concentration of H_2O is essential for Li-ion batteries, for our core/shell nanoparticles a compromise between smallest useful particle size and minimum water residual has to be found.

Electrochemical properties

Finally, the cyclic voltammograms in Fig. 7 show that efforts undertaken, combining optimized coating of the

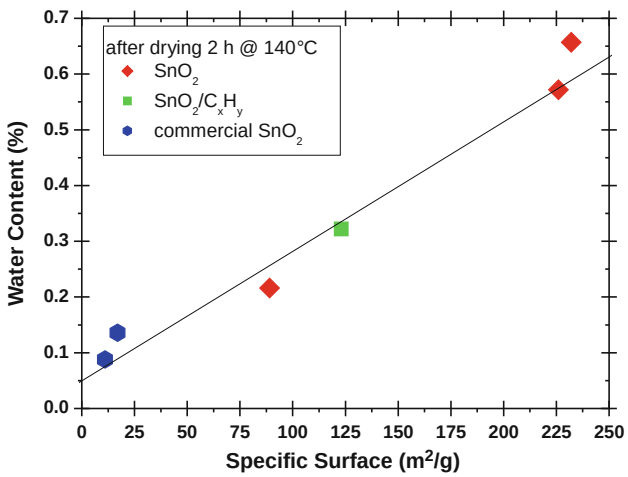

Fig. 6 Water content (measured by coulometric water titration) as a function of specific surface area (determined by BET) for different SnO_2 and SnO_2/C_xH_y powders. The residual water content is linearly correlated to the specific surface area

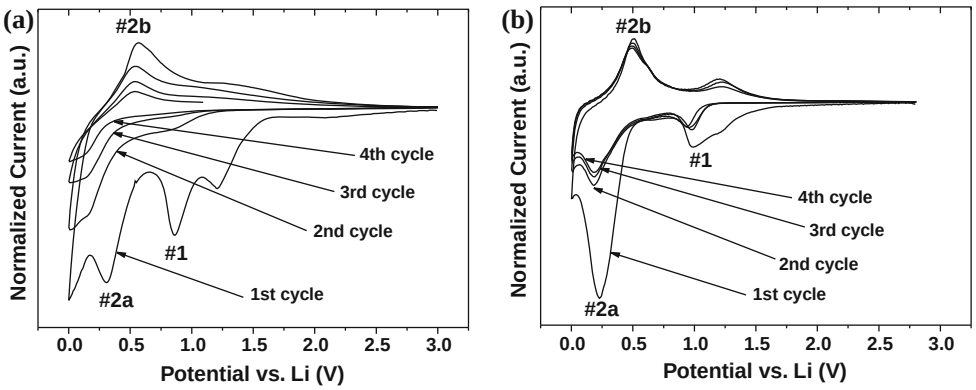

Fig. 7 Normalized cyclic voltammograms, showing the irreversible peak at 0.8 V (#1), due to the irreversible reaction $SnO_2 + 4Li \rightarrow Sn + 2Li_2O$, the alloy formation Li_xSn at 0.4 V (#2a) and the de alloying at 0.5 V (#2b). **a** Swagelok cell using anode material made of SnO_2 nanoparticle film (transport in atmosphere, no heating). The material shows the typical peaks, but also a distinct fading after the first cycle. **b** Swagelok cell using anode material made of SnO_2/C_xH_y nanoparticle film (transport under inert conditions, additional heating). As in the case of SnO_2, expected peaks appear, but fading is significantly reduced

SnO_2 nanoparticles, together with sample transport into glove box under inert conditions straight after synthesis, are successful. The SnO_2 electrode (Fig. 7a) was used as produced (with air contact during transport to glove box, no drying), and compared to the SnO_2/C_xH_y electrode (Fig. 7b), which was transported in Ar and additionally dried. For better visualization data are normalized. During the first cycle both materials exhibit the irreversible peak at 0.8 V, which can be ascribed to the irreversible reaction $SnO_2 + 4Li \rightarrow Sn + 2Li_2O$ (peak labeled #1). During this reaction metallic Sn is formed, being responsible for current decrease. The discharging occurs at 0.4 V (peak labeled #2a) and corresponds to the alloy formation Li_xSn. The de-alloying occurs at approximately 0.5 V (peak labeled #2b), which corresponds to the charging of the half-cell. The global reaction (#2a, #2b) can be described by the reaction $Sn + xLi \leftrightarrow Li_xSn$, and is reversible. The theoretical maximum amount of Li-ions which can be inserted is 4.4 Li-ions per Sn. During this alloying/de-alloying process volume changes occur, often leading to a fading of the anode with increasing cycling. In Fig. 7, this is observed for the bare SnO_2 anode where the curves for the 2nd and 4th cycle are clearly differing. In contrast, the fading of SnO_2/C_xH_y is significantly reduced as the curves for the 2nd 4th cycle are close to each other. This significant reduction of fading is assumed to be a combined effect of encapsulation of SnO_2 by the C_xH_y shell, and the complete handling of the anode in inert atmosphere. Our results for SnO_2/C_xH_y anodes (binder-free, no additional carbon black) are in good agreement with cyclovoltammetry shown in literature for various SnO_2/C systems [7, 13, 48, 49]. The broad peak noticed for the SnO_2/C_xH_y anode (Fig. 7b) during charging at a voltage around 1.3 V can be attributed to reforming of SnO_2. Together with the discharge peak labeled #1, a partially reversible reaction $SnO_2 \leftrightarrow Sn$ is observed [4, 48, 50, 51]. Therefore, this reaction is considered as quasi-reversible.

Figure 8a shows the galvanostatic charge/discharge curves for the first cycle, and Fig. 8b compares the specific charge/discharge capacity as a function of cycle number for the two sets of anode materials in a half-cell, SnO_2 nanoparticle films and SnO_2/C_xH_y core/shell nanoparticle films, in the as-produced state (with air contact during transport to glove box, no drying) and after drying at 140 °C for 2 h, respectively. The initial discharge capacities are 1260 and 1749 mAh/g for the as-produced and dried bare SnO_2 anode material, and 3065 and 3689 mAh/g for the as-produced and dried SnO_2/C_xH_y anode materials, respectively. The 2nd discharge capacities for these materials are 684, 819, 1382, and 1469 mAh/g. The differences of capacities from the 1st 2nd cycle are due to the formation process of Sn due to reduction of SnO_2 and the development of a solid electrolyte interface (SEI).

The corresponding charge capacities for the 1st cycle are 690 and 707 mAh/g, and 985 and 1138 mAh/g, respectively. In the 2nd charge cycle 628, 709, 928, and 1150 mAh/g are observed. The specific discharge capacities are greater than the specific charge capacities, suggesting that not only Li intercalation into Sn contributes to the capacity. As has been shown in Fig. 1, the nanoparticle layers are porous. It is known that Li^+ can also be stored into pores [51, 52], leading to higher discharge capacities. For the bare anode material a difference between discharge and charge capacity is not anymore observable beyond the 10th cycle, whereas for the SnO_2/C_xH_y anodes this threshold is only observed beyond the 30th cycle. We assume the coated material has a higher porosity, hindering a complete delithiation.

The influence of adsorbed water on the specific capacity, as well as the influence of coating the SnO_2 nanoparticles

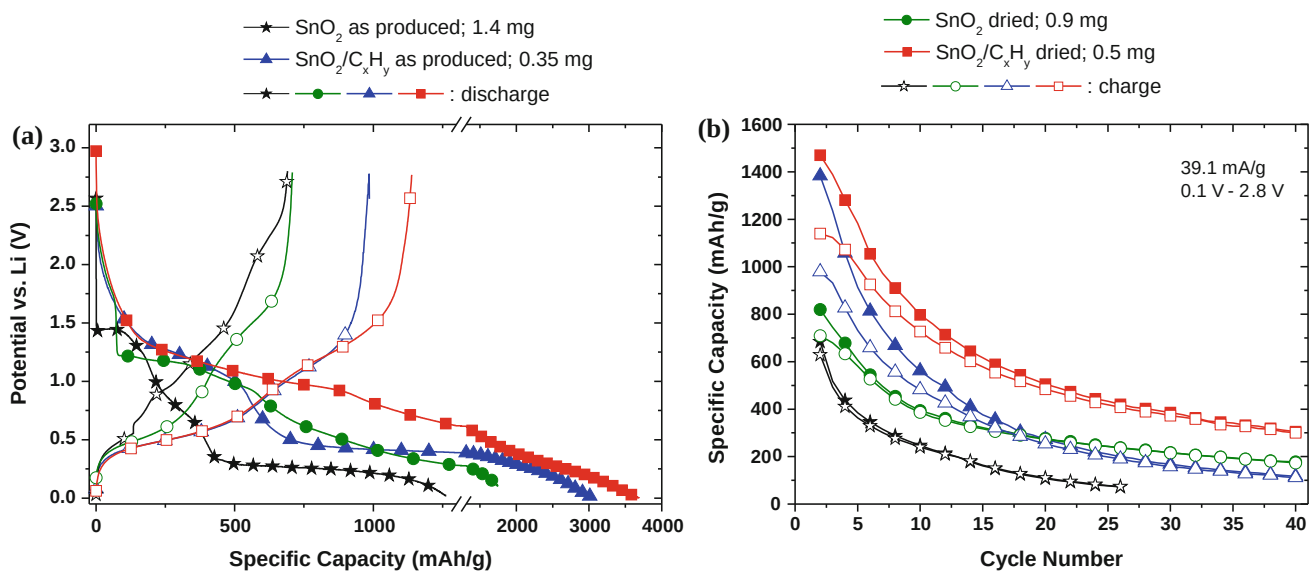

Fig. 8 Influence of sample treatment on specific capacity as a function of cycle number for anodes made with SnO_2 nanoparticles films and anodes made with SnO_2/C_xH_y core/shell nanoparticle films. **a** Charge/discharge capacity for the first cycle. The specific capacity of the as produced anodes (*filled symbols*) is significantly lower than the specific capacity of the heat treated anodes (*open symbols*). **b** Discharge and charge capacities as a function of cycling

with C_xH_y can clearly be seen from these figures. Comparing the capacities of dried SnO_2 and dried SnO_2/C_xH_y, a difference of approximately 130 mAh/g can be observed in the 40th cycle. Drying improves the specific capacity and reduces the fading for both, the bare SnO_2 and the core/shell SnO_2/C_xH_y based anodes. Additional coating of SnO_2 with C_xH_y obviously further improves the specific capacity. Such enhancing effects are known for amorphous carbon [6, 49, 53] being gable to store Li^+. We assume that the C_xH_y coating is amorphous and therefore also enhances Li^+ intercalation. Furthermore, the quasi-reversible reaction $SnO_2 \leftrightarrow Sn$ also contributes to enhanced capacity [51, 52]. Nevertheless, a significant fading of the material is observed. Although the size of the bare SnO_2 nanoparticles is in the optimum size range [54] for nanoparticles in Li-ion batteries, and the slightly larger core/shell particles contain an inherent buffer layer improving the capacities, fading is not reduced yet. This is attributed to internal stresses caused by the volume change and aggregation of Sn resulting in loss of active material.

Summary and conclusions

We apply a versatile microwave plasma process for the synthesis of SnO_2-based core/shell nanoparticles and their in situ deposition on Ni-substrates for application as anode materials in Li-ion battery. The combination of different microscopic and spectroscopic methods, as e.g., TEM, SEM, XRD, or XPS is elementary to characterize particles and films. The core particles always crystallize in the tetragonal cassiterite structure, with a primary particle size below 10 nm. Increasing microwave power reduces the amount of carbonaceous material stemming from residual precursor, so that "clean" SnO_2 nanoparticles enter the second plasma stage for the coating step. With XPS an increase in carbon components is found with increasing C precursor feed, being a proof for increasing C_xH_y coating.

Atmospheric adsorbents can be reduced while applying heat treatment, and/or by handling samples and materials in inert gas. The necessary efforts are more laborious the smaller the particles are. Optimization with respect to nanoparticle synthesis and nanoparticle film deposition is necessary, combined with transport of the anodes under inert conditions and improved cell mounting.

The microscopic and spectroscopic investigations have shown that it is possible to synthesize SnO_2 and SnO_2/C_xH_y nanoparticles with microwave plasma synthesis, using $Sn(C_4H_9)_4$ and $C_{10}H_{12}$ as precursors in an Ar/20% O_2 plasma. An increased discharge capacity, compared to bulk SnO_2, was shown for the coated material. The significant influence of adsorbed water on the specific capacities was elaborated. We expect this influence also being present in a material with improved cycling stability. Although the shell is not graphitic yet, a principal improved functionality of the Swagelok half-cells based on SnO_2/C_xH_y core/shell nanoparticles, and mounted with anodes transported in inert atmosphere, has been demonstrated. Obviously, nanostructured SnO_2 combined with C_xH_y coating is not efficient enough to improve cycling stability. Therefore, elemental

carbon in form of graphite or graphene is needed. To synthesize elemental carbon in the plasma, preferentially in the form of graphite, inert gas plasma obviously is necessary and is subjected to further investigations.

Acknowledgements The authors acknowledge financial support by the German Ministry for Education and Research, project "Battery Competence Consortium South Electrochemistry for Electromobil ity" under contract number 03KP801.

References

1. Li N, Martin CR, Scrosati B (2001) J Power Sources 97 98:240
2. Wang Y, Lee JY, Chen BH (2004) J Electrochem Soc 151(4):A563. doi:10.1149/1.1647571
3. Wang Y, Lee JY (2005) J Power Sources 144(1):220
4. Zhao Y, Zhou Q, Liu L, Xu J, Yan M, Jiang Z (2006) Electrochim Acta 51(13):2639
5. Liang Y, Fan J, Xia X, Jia Z (2007) Mater Lett 61(22):4370. doi: 10.1016/j.matlet.2007.02.008
6. Aifantis KE, Brutti S, Hackney SA, Sarakonsri T, Scrosati B (2010) Electrochim Acta 55(18):5071. doi:10.1016/j.electacta. 2010.03.083
7. Gao M, Chen X, Pan H, Xiang L, Wu F, Liu Y (2010) Electro chim Acta 55(28):9067. doi:10.1016/j.electacta.2010.08.033
8. Ochs R, Szabó DV, Schlabach S, Becker S, Indris S (2011) Phys Status Solidi A 208(2):471. doi:10.1002/pssa.201026652
9. Ohzuku T, Iwakoshi Y, Sawai K (1993) J Electrochem Soc 140(9):2490. doi:10.1149/1.2220849
10. Bruce PG, Scrosati B, Tarascon JM (2008) Angew Chem Int Ed 47(16):2930
11. Centi G (2009) Europ J Inorg Chem 26:3851
12. Chen Y C, Chen J M, Huang Y H, Lee Y R, Shih HC (2007) Surf Coat Technol 202(4 7):1313
13. Yao J, Shen X, Wang B, Liu H, Wang G (2009) Electrochem Commun 11(10):1849
14. Du Z, Yin X, Zhang M, Hao Q, Wang Y, Wang T (2010) Mater Lett 64(19):2076
15. Qiao H, Zheng Z, Zhang L, Xiao L (2008) J Mater Sci 43(8):2778. doi:10.1007/s10853 008 2510 8
16. Vollath D, Szabó DV (2006) J Nanopart Res 8(3 4):417. doi: 10.1007/s11051 005 9014 0
17. Schumacher B, Ochs R, Tröße H, Schlabach S, Bruns M, Szabó DV, Haußelt J (2007) Plasma Process Polym 4(S1):S865. doi: 10.1002/ppap.200732101
18. Dato A, Radmilovic V, Lee Z, Phillips J, Frenklach M (2008) Nano Lett 8(7):2012. doi:10.1021/nl8011566
19. Marcinek M, Hardwick LJ, Zukowska GZ, Kostecki R (2010) Carbon 48(5):1552
20. Moreno Couranjou M, Monthioux M, Gonzalez Aguilar J, Fulc heri L (2009) Carbon 47(10):2310
21. Peter S, Günther M, Hauschild D, Grambole D, Richter F (2010) Vacuum 85(4):510. doi:10.1016/j.vacuum.2010.10.006
22. Koprinarov N, Konstantinova M (2011) J Mater Sci 46(5):1494. doi:10.1007/s10853 010 4951 0
23. Park M, Kang Y, Kim J, Wang G, Dou S, Liu H (2008) Carbon 46(1):35. doi:10.1016/j.carbon.2007.10.032
24. Parry KL, Shard AG, Short RD, White RG, Whittle JD, Wright A (2006) Surf Interface Anal 38(11):1497. doi:10.1002/sia.2400
25. Scofield JH (1976) J Electron Spectrosc Relat Phenom 8(2):129. doi:10.1016/0368 2048(76)80015 1
26. Tanuma S, Powell CJ, Penn DR (1994) Surf Interface Anal 21(3):165. doi:10.1002/sia.740210302
27. Schlabach S, Szabó DV, Vollath D, de la Presa P, Forker M (2007) J Alloy Compd 434:590. doi:10.1016/j.jallcom.2006.08. 087
28. Schlabach S, Szabó DV, Vollath D, Braun A, Clasen R (2004) Funct Nanomater Optoelectronics Other Appl 99 100:191
29. Vollath D, Szabó DV (2002) In: Choy K L (ed) Innovative pro cessing of films and nanocrystalline powders. Imperial College Press, London, p 219
30. Brossmann U, Sagmeister M, Polt P, Kothleitner G, Letofsky Papst I, Szabó DV, Würschum R (2007) Phys Status Solidi RRL 1(3):107. doi:10.1002/pssr.200701019
31. Szabó DV, Schlabach S, Ochs R (2007) In: Gemming T, Hart mann U, Mestres P, Walther P (eds) Microscopy Conference 2007, Saarbrücken, Germany, 2007. Microscopy and Analysis. Cambridge University Press, vol 13, Supplement 3 p 430
32. Fuchs M, Breitenstein D, Fartmann M, Grehl T, Kayser S, Ko ester R, Ochs R, Schlabach S, Szabó DV, Bruns M (2010) Surf Interface Anal 42(6 7):1131
33. Vollath D, Szabó DV, Schlabach S (2004) J Nanopart Res 6(2 3):181
34. Lamparth I, Szabó DV, Vollath D (2002) Macromol Symp 181:107
35. Szabó DV, Lamparth I, Vollath D (2002) Macromol Symp 181:393
36. Powell RA (1979) Appl Surf Sci 2:397
37. Hoflund GB, Corallo GR (1992) Phys Rev B 46(11):7110
38. JCPDS 41 1445. The International Centre for Diffraction Data, Newton Square, PA, USA
39. Yu KN, Xiong YH, Liu YL, Xiong CS (1997) Phys Rev B 55(4):2666
40. Lock EH, Petrovykh DY, Mack P, Carney T, White RG, Walton SG, Fernsler RF (2010) Langmuir 26(11):8857. doi:10.1021/ la9046337
41. Stevens JS, Schroeder SLM (2009) Surf Interface Anal 41(6):453. doi:10.1002/sia.3047
42. Stankovich S, Piner RD, Chen X, Wu N, Nguyen ST, Ruoff RS (2006) J Mater Chem 16(2):155
43. Li F, Song J, Yang H, Gan S, Zhang Q, Han D, Ivaska A, Niu L (2009) Nanotechnology 20(45):455602
44. Moulder JF, Stickele WF, Sobol PE, Bomben KD (1992) Hand book of X ray photolelectron spectroscopy. Perkin Elmer Corp., Eden Prairie
45. Trouillet V, Tröße H, Bruns M, Nold E, White RG (2007) J Vac Sci Technol A 25(4):927. doi:10.1116/1.2731342
46. Ma Y, Castro RHR, Zhou W, Navrotsky A (2011) J Mater Res 26(7):848. doi:10.1557/jmr.2010.97
47. Mersmann A, Kind M, Stichlmair J (2005) Thermische Verfah renstechnik, 2nd edn. Springer, Berlin
48. Liu HP, Long DH, Liu XJ, Qiao WM, Zhan L, Ling LC (2009) Electrochim Acta 54(24):5782. doi:10.1016/j.electacta.2009.05. 030
49. Hassoun J, Derrien G, Panero S, Scrosati B (2008) Adv Mater 20(16):3169. doi:10.1002/adma.200702928
50. Mohamedi M, Lee S J, Takahashi D, Nishizawa M, Itoh T, Uchida I (2001) Electrochim Acta 46(8):1161. doi:10.1016/s0013 4686(00)00702 7
51. Demir Cakan R, Hu Y S, Antonietti M, Maier J, Titirici M M (2008) Chem Mater 20(4):1227. doi:10.1021/cm7031288
52. Deng D, Lee JY (2008) Chem Mater 20(5):1841. doi:10.1021/ cm7030575
53. Sun X, Liu J, Li Y (2006) Chem Mater 18(15):3486. doi: 10.1021/cm052648m
54. Kim C, Noh M, Choi M, Cho J, Park B (2005) Chem Mater 17(12):3297. doi:10.1021/cm048003o

Karlsruher Institut für Technologie

OPEN ACCESS

Repository KITopen

Dies ist ein Postprint/begutachtetes Manuskript.

Empfohlene Zitierung:
Szabo, D. V.; Kilibarda, G.; Schlabach, S.; Trouillet, V.; Bruns, M.
Structural and chemical characterization of SnO_2-based nanoparticles as electrode material in Li-ion batteries
2012. Journal of materials science, 47.
doi: 10.554/IR/110086182

Zitierung der Originalveröffentlichung:

Szabo, D. V.; Kilibarda, G.; Schlabach, S.; Trouillet, V.; Bruns, M.
Structural and chemical characterization of SnO_2-based nanoparticles as electrode material in Li-ion batteries
2012. Journal of materials science, 47, 4383–4391.
doi: 10.1007/s10853-012-6292-7

Lizenzinformationen: KITopen-Lizenz